# Autocalibration method for guided wave tomography with undersampled data

Tom Druet, Jean-Loup Tastet, Bastien Chapuis, Emmanuel Moulin

Version of Record: https://www.sciencedirect.com/science/article/pii/S0165212518301781
Manuscript_7faeba7d68d2efe88adaa48b5a211b28

# Autocalibration Method for Guided Wave Tomography with Undersampled Data

Tom Druet[a], Jean-Loup Tastet[a,c], Bastien Chapuis[a], Emmanuel Moulin[b]

[a] *CEA, LIST, F-91191 Gif-sur-Yvette, France*
[b] *IEMN UMR CNRS 8520, Université Polytechnique Hauts-de-France, F-59313 Valenciennes cedex 9, France*
[c] *Now at Discovery Center, Niels Bohr Institute, Blegdamsvej 17, Copenhagen, Denmark*

**Abstract**

This paper presents a baseline-free quantitative method for the imaging of corrosion flaws present in thin plates with under-sampled data. This method is based on the Hybrid Algorithm for Robust Breast Ultrasound Tomography (HARBUT) which is itself inherently baseline-free. However, in order to ensure that the incident field component becomes negligible in the reconstruction, a calibration step is necessary. Indeed, it is essential to rescale the data with respect to the acoustic model whether it be simulation data or experimental data. This calibration is usually performed by manually choosing a ray for which the domain of propagation is assumed sound. This can be problematic because this method is not automatic. Moreover, if the chosen ray happens to pass through a flaw, the resulting image will be of poor quality. This paper proposes an autocalibration method for the rescaling step. The field of application is Structural Health Monitoring (SHM) of critical structures with heavy constraints on both sensor intrusiveness and diagnostic reliability. In order to limit intrusiveness, a sub-sampled array of embedded guided waves sensors within the structure is used. Extensions to HARBUT are introduced to compensate for the aliasing caused by the undersampling. The benefits of these extensions are then assessed with numerical simulations and experimental datasets measured by a PZT network.

*Keywords:* Structural health monitoring, Guided waves, Ultrasound tomography, Piezoelectric transducers, Baseline-free

## 1. Introduction

In most industries, corrosion can be disastrous if not correctly monitored. Structural Health Monitoring (SHM) is "the process of acquiring and analyzing data from on-board sensors to evaluate the health of a structure." (see [1] page 4). Guided wave tomography is a promising SHM solution to monitor corrosion. Actually, it is an imaging method studied since many decades, allowing to estimate the remaining wall thickness of corrosion patches in plates, pipes, or more complicated structures. Several algorithms, based on different physical phenomena, have been developed, the older being straight-ray tomography [2–5]. This class of algorithms assumes the velocity field to be very weakly non-uniform, thus neglecting refraction and diffraction. Another ray-tomography algorithm, named bent-ray, takes into account the wave field refracted by the potential defect [6–9]. This means that very large, non-diffracting defects can be imaged. A different approach is proposed by diffraction tomography (DT) algorithms [10–14]. These algorithms are based on the Born approximation and allow to image small defects. More recently, an hybrid algorithm named Hybrid Algorithm for Robust Breast Ultrasound Tomography (HARBUT) has been proposed by Huthwaite and Simonetti [15] in 2013 and was then followed by many developments [16–20].

The work presented in this paper proposes several extensions to HARBUT in order to satisfy the heavy constraints imposed by the SHM framework, such as sensor intrusiveness and diagnostic reliability. To satisfy the former constraint, one has to reduce the number of sensors embedded in the structure. Indeed, guided wave tomography needs many sensors and it is known that PZT transducers can be intrusive because of their size and electrical wires. A way of

*Email addresses:* tom.druet@cea.fr (Tom Druet), bastien.chapuis@cea.fr (Bastien Chapuis), emmanuel.moulin@univ-valenciennes.fr (Emmanuel Moulin)

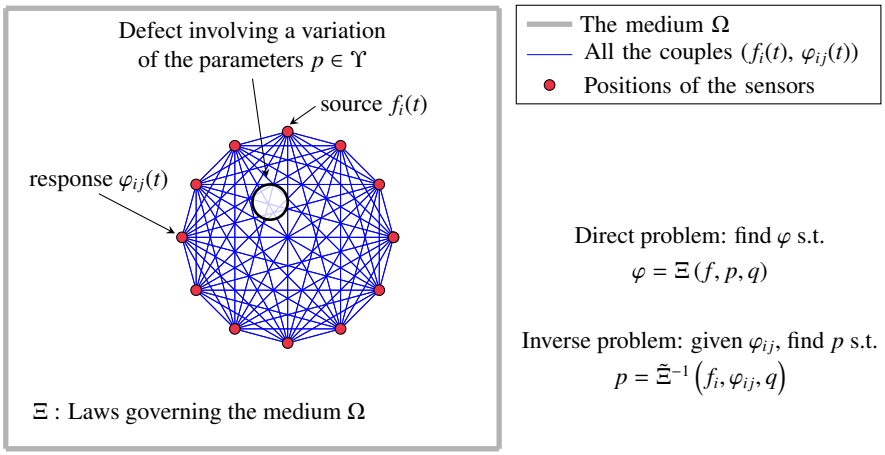


**Fig. 1.** Inverse problem to solve with guided wave tomography.

preserving the robustness of the algorithm as the number of sensors decreases is presented in this paper. Concerning the latter constraint (the diagnostic reliability), it is well known in SHM that baseline-free methods could decrease tremendously the number of false alarms, typically caused by temperature changes or the ageing of sensors between two measurements. This paper presents an autocalibration method coupled to HARBUT. HARBUT is itself inherently baseline-free but the calibration step is usually performed either manually by choosing a ray for which the domain of propagation is assumed sound or by using a baseline measurement which increases the risk of false alarms. The calibration method presented in this paper is automatic and thus adapted to the SHM context.

This paper is organized as follows. Section 2 presents the extensions of the original iterative HARBUT described in [15], such as the convergence criterion and several added or modified regularization methods (Gaussian filter, threshold based on physical considerations and variable relaxation). Section 3 presents tomographic reconstructions based on the original and modified algorithms with simulated data which take into account the PZT transducers behavior. Three defects involving either refraction or diffraction phenomena are considered. Finally, in Section 4, the method is validated on experimental data measured on a real 2 mm thick aluminum plate. Note that throughout this paper all tomographies are performed with the $A_0$ mode.

## 2. Method

A direct problem consists in finding the response $\varphi(\boldsymbol{x}, t)$ for a given source $f(\boldsymbol{x}, t), \forall(\boldsymbol{x}, t) \in \Omega \times \mathbb{R}$ given the laws $\Xi$ governing the medium $\Omega$ (Fundamental principle of dynamics, Hooke's law) and the parameters of the problem $(q, p) \in \Upsilon_0 \times \Upsilon$ for some parameter spaces $\Upsilon_0$ and $\Upsilon$ (characteristics of the material, geometry). Guided wave tomography consists in finding some of the parameters $p \in \Upsilon$ (here, the thickness of the plate) given the laws $\tilde{\Xi}^{-1}$ governing the medium, the other parameters $q \in \Upsilon_0$ (characteristics of the material) and a partial response $\varphi_{ij}(t)$ for a given source $f_i(t)$; it is an inverse problem. Note that $\tilde{\Xi}$ is an invertible regularization of $\Xi$. Fig. 1 is a representation of the problem considered in this article. Sensors are positioned on a circle. $i$ and $j$ correspond to the sensor indices for an emission $i$ and a measurement $j$. The partial responses $\varphi_{ij}(t)$ are the inputs to the guided wave tomography. These partial responses are measured for all the couples represented with thin blue lines on Fig. 1. Guided wave tomography consists in inverting these measurements in order to obtain a quantitative image of the plate thickness.

In order to solve the inverse problem, guided wave tomography is usually based on a simplified model of guided wave propagation in order to avoid a prohibitive computation time. An acoustic model is generally used, which is characterized by a scalar wave equation and a dispersion relation $\omega(k)$ for the chosen guided wave mode, $A_0$ in this paper. The original iterative HARBUT [15] is used here to solve the inverse problem.

The original iterative HARBUT [15] uses a ray-tomography as a first estimation of the plate thickness, in order to respect the Born approximation in the subsequent DT step. In this section, the differences between the original

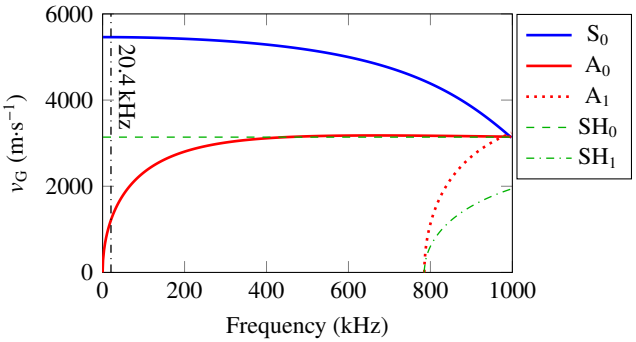


**Fig. 2.** Dispersion curves of the group velocity $v_G$ for $S_0$, $A_0$, $A_1$, $SH_0$ and $SH_1$, and for a 2 mm thick aluminum plate ($V_L$ = 6360 m s$^{-1}$, $V_T$ = 3140 m s$^{-1}$ and $\rho$ = 2.7 g cm$^{-3}$).

HARBUT and our method are presented. Some additional elements are also introduced, such as a regularization method called "variable relaxation", which helps to limit aliasing effects with strongly undersampled data.

### *2.1. Algorithmic differences with the original iterative HARBUT*

This section includes two parts; first are presented some differences for the Time-of-Flight (ToF) tomography step and then for the DT one.

#### *2.1.1. Time-of-Flight Tomography step*

Whether it be straight-ray or bent-ray, in order to solve the propagation problem, one uses the SART algorithm [21] (or FMM-SART for bent-ray [6]). The structure to be imaged is represented at the position $\boldsymbol{x}$ by the scalar slowness field $s(\boldsymbol{x}) = \frac{1}{v_G(\boldsymbol{x})}$ (isotropic material), where $v_G$ is the group velocity. Fig. 2 presents the dispersion curves of the group velocity for the configuration presented in this paper (the working product *frequency* × *thickness* considered in this paper is very low: 40.8 kHz mm). To represent the slowness $s(\boldsymbol{x})$, we project it on a finite basis. In the original bent ray algorithm [6], a basis of cubic or spherical pixels / voxels is used for the reconstruction, and a non-interpolating B-spline filter [22] is applied a posteriori in order to accurately estimate the gradient when computing the rays. Here, we have instead expressed the SART algorithm in terms of B-splines from the very beginning. The projection $\tilde{s}(\boldsymbol{x})$ of the scalar slowness thus reads:

$$\tilde{s}(\boldsymbol{x}) = \sum_{i,j} S_{ij}\beta_{ij}(\boldsymbol{x}), \tag{1}$$

where $\beta$ is a 2D B-spline basis and $S_{ij}$ is the coefficient associated to the B-spline $\beta_{ij}$.

With this decomposition, it is now possible to express the ToF $\tau_{k\to l}$ along the trajectory (straight or bended) $\gamma_{k\to l}$ between the emitter $k$ and the receiver $l$:

$$\tau_{k\to l} = \int_{\gamma_{k\to l}} s(\gamma)\,\mathrm{d}\gamma \cong \int_{\gamma_{k\to l}} \tilde{s}(\gamma)\,\mathrm{d}\gamma = \int_{\gamma_{k\to l}} \sum_{i,j} S_{ij}\beta_{ij}(\gamma)\,\mathrm{d}\gamma = \sum_{i,j} S_{ij}A_{ijkl}, \tag{2}$$

where $A_{ijkl} = \int_{\gamma_{k\to l}} \beta_{ij}(\gamma)\,\mathrm{d}\gamma$ is the contribution of the basis element $\beta_{ij}$ to the ToF $\tau_{k\to l}$.

The use of B-splines allows us to obtain smooth images, which is important for the following DT iterations. In practice, fourth order splines are used. This is a good compromise to get a smooth-enough image while keeping a sufficiently small support for the defect reconstruction.

To perform baseline-free tomography, only ToFs corresponding to the defect data are available: $\tau^{\text{defect}}_{k\to l}$. Therefore, an absolute estimator needs to be used, and is described here. The n$^{\text{th}}$ iteration of the ray-tomography step reads:

$S_{ij}^{(n)} = S_{ij}^{(n-1)} + \delta_k S_{ij}^{(n)}$, where $\delta_k S_{ij}^{(n)}$ is the correction applied to the coefficient $S_{ij}$ and is calculated according to the following formulation:

$$\delta_k S_{ij}^{(n)} = \frac{1}{N_{ij}} \sum_l \left( W_{ijkl} \frac{\tau_{k\to l}^{\text{defect}} - \tau_{k\to l}^{(n-1)}}{\lambda_{k\to l}} \right), \tag{3}$$

where $\lambda_{k\to l}$ is the trajectory length, $W_{ijkl}$ is equal to $A_{ijkl}$ in the simplest case but usually includes a Hamming window to avoid side effects, and the normalization factor $N_{ij}$ reads: $N_{ij} = \sum_l A_{ijkl}$.

Unlike the absolute estimator, the relative estimator uses the ToF corresponding to baseline data: $\tau_{k\to l}^{\text{baseline}}$. The relative estimator allows to eliminate some systematic errors due to experimental uncertainties and works on relative ToF. The idea is to subtract independently the experimental ToF ($\tau_{k\to l}^{\text{defect}}$ and $\tau_{k\to l}^{\text{baseline}}$) and the calculated ToF ($\tau_{k\to l}$ and $\tau_{k\to l}^{\text{healthy}}$). The relative estimator is then calculated according to the following formulation:

$$\delta_k S_{ij}^{(n)} = \frac{1}{N_{ij}} \sum_l \left( W_{ijkl} \frac{(\tau_{k\to l}^{\text{defect}} - \tau_{k\to l}^{\text{baseline}}) - (\tau_{k\to l}^{(n-1)} - \tau_{k\to l}^{\text{healthy}})}{\lambda_{k\to l}} \right). \tag{4}$$

Those two estimators are compared on experimental data in Section 4.2.1.

Finally, concerning the ray-tomography, a regularization method - presented in Section 2.2 - is applied to the map at every iteration in order to obtain a "cleaner" ray-tomography image for the subsequent DT iterations.

### 2.1.2. *Diffraction Tomography step*

Concerning the DT step, the algorithm used in this paper is the same as the original HARBUT. However, several extensions to HARBUT are proposed in order to satisfy the heavy constraints imposed by the SHM framework, such as sensor intrusiveness and diagnostic reliability. Specifically, a Gaussian blur adapted to the undersampled data is applied between iterations and an autocalibration method is used to automate the imaging procedure.

*Prerequisite.* The same object function $\mathrm{O}(\boldsymbol{x})$ as in [15] is used to represent the image:

$$\mathrm{O}(\boldsymbol{x}) = k(\boldsymbol{x})^2 - k_0^2 = k_0^2 \left( \left( \frac{v_0}{v(\boldsymbol{x})} \right)^2 - 1 \right), \tag{5}$$

where $k_0$ is the background wavenumber, $v_0$ the background phase velocity and $v(\boldsymbol{x})$ the phase velocity at the position $\boldsymbol{x}$, which is linked to the thickness thanks to the dispersion curves when the algorithm has converged. Iterative HARBUT consists in calculating iteratively the correction $\mathrm{O}_\delta(\boldsymbol{x})$, which is added to the previous estimation $\mathrm{O}_b(\boldsymbol{x})$ so that $\mathrm{O}(\boldsymbol{x}) = \mathrm{O}_b(\boldsymbol{x}) + \mathrm{O}_\delta(\boldsymbol{x})$. The correction $\mathrm{O}_\delta(\boldsymbol{x})$ is calculated by means of a beamforming image for which a filter in the spatial frequency domain (see [15] for details) is applied. In the HARBUT theory, the input data is the diffracted field but it is shown in [18] how it is possible to work with the total field instead of the diffracted field. This is the key step for HARBUT to be free of any baseline.

*Autocalibration method.* In order to perform HARBUT, it is essential to rescale the data with respect to the theoretical model in order for the incident field component to become negligible in the reconstruction, whether it be simulation data or experimental data. This calibration could be done thanks to a baseline but as explained before, this is unwanted in the case of a SHM application because of the false alarms which could occur. This is why the calibration is usually made with the current measurements, by manually choosing a ray for which the domain of propagation is assumed sound. This is not ideal either in SHM because it is not automatic. Moreover, if the chosen ray passes through a flaw, the resulting image will be of poor quality. Here, an autocalibration method is proposed. This method makes the global imaging process automatic and baseline-free while preserving its robustness.

The theoretical incident field is given by the non-perturbed Green's function:

$$G_0(\boldsymbol{x}; \boldsymbol{x}') = -\frac{i}{4} H_0^{(1)}(k_0 |\boldsymbol{x} - \boldsymbol{x}'|), \tag{6}$$

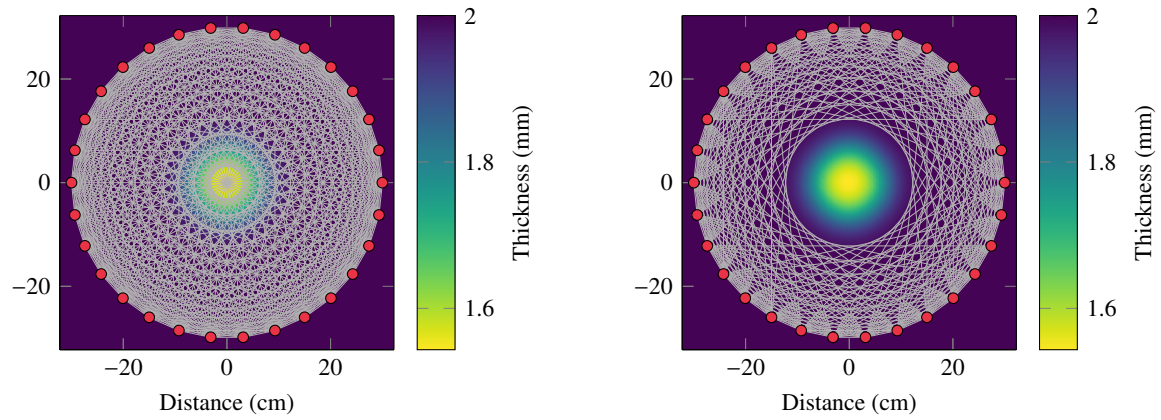


(a) Full ray distribution usually used on baseline data in order to calibrate the field in classic calibration.

(b) All the rays used in order to calibrate the field with the autocalibration method presented un this paper.

**Fig. 3.** Rays crossing the defect area after straight-ray tomography reconstruction.

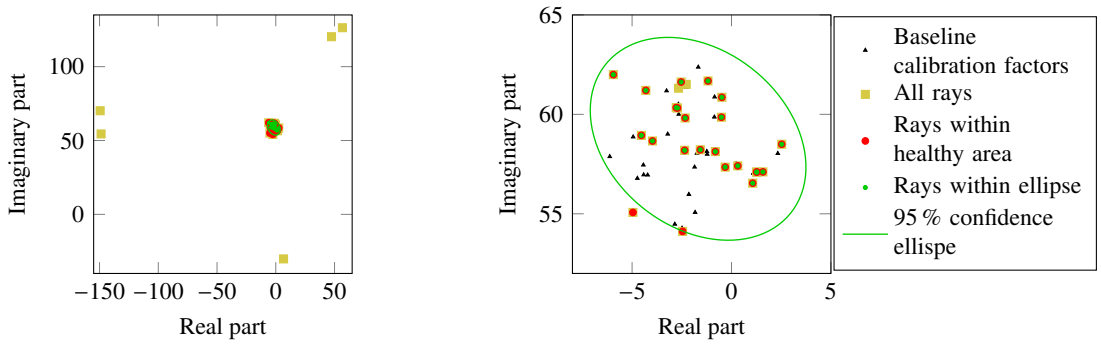


(a) All calibration factors.

(b) Zoom in on the 95 % confidence ellipse.

**Fig. 4.** Calibration factors plotted in the complex plane.

where $H_0^{(1)}$ is the Hankel function of the first kind and of zeroth order. The idea is to calculate the calibration factors $c_{ij}$:

$$c_{ij} = \frac{G_0(\boldsymbol{x}_i; \boldsymbol{x}_j)}{\varphi_i^{\text{healthy}}(\boldsymbol{x}_j)}, \tag{7}$$

where the index $i$ denotes the emitter, the index $j$ the receiver and $\varphi^{\text{healthy}}$ the measured incident field. Then these calibration factors are multiplied to the measured data, which provides the input calibrated fields for HARBUT. In the case of tomography relying on baseline signals, the construction of $\varphi^{\text{healthy}}$ is straightforward, but for a baseline-free method it is challenging to do it in a robust way. Naively, we could select a couple $(i, j)$ for which the ray crosses no defect and then proceed to the calibration with only this couple. This leads to two problems: the first one is that when experimental uncertainties are too strong this approach could introduce noise in the resulting image; the second one is that it is difficult in practice — even nearly impossible — to be sure that there is no defect on the path of the ray, and this would strongly disrupt the rescaling process. Actually, even if a first ray-tomography using the absolute estimator is performed to approximately locate potential defects, this kind of algorithm is not able to detect diffracting defects. Therefore, it has been decided to develop a method to construct the $c_{ij}$ in a robust way without any baseline.

The $c_{ij}$ are constructed in three steps:

1. A ray-tomography with absolute estimator is performed with enough regularization (presented in Section 2.2) to obtain a background without noise. Fig. 3a presents a result of this kind of tomography with all the rays corresponding to all possible couples $(i, j)$. Fig. 4 shows all the potential $c_{ij}$ of Eq. (7) for baseline data (black triangles) and for defect data (yellow squares). Obviously, the baseline calibration factors are in close proximity to each other, and concerning the potential calibration factors corresponding to the defect state, it is possible to see some of them which diverge from the others. They correspond to the rays which cross the defect. Moreover, the problem is axisymmetric, which implies that if $n_{\text{sensors}}$ is the number of sensors in the distribution, for each visible point there are $n_{\text{sensors}}$ points superimposed. The non axisymmetric case is treated in Fig. 19 for experimental data.
2. For each ray, we verify that the ray is not crossing any visible defect on the ray-tomography along its path (in practice, a threshold of 1 % relative to the healthy thickness has been used). If a ray crosses a defect, it is not used in the following step. This means that $m$ rays are kept with $m \leq n_{\text{rays}}$ where $n_{\text{rays}} = \frac{n_{\text{sensors}}(n_{\text{sensors}}-1)}{2}$ the total number of rays. Fig. 3b shows the $m$ remaining rays. Fig. 4 shows the corresponding $c_{ij}$ (red circle). This time, the factors kept are in close proximity to each other. It is possible to notice that only $2\,n_{\text{sensors}}$ factors were discarded (two red circles are not superimposed on yellow squares) despite being in close proximity, which suggests that the threshold may be too strict, but this is preferable to the contrary.
3. Finally, a confidence ellipse is computed based on the factors corresponding to the rays within the healthy area (red circles). As noticed before, the ray-tomography algorithms are blind to diffraction. This means that it is possible for a small defect to be within the healthy area, intersecting some of the kept trajectories. Fortunately, the associated calibration factors should diverge from the "proximity area" and thus be outside the confidence ellipse. In this paper, a 95 % confidence ellipse has been chosen but we have tested smaller values, down to 5 %, and the global error of the resulting image does not change significantly. Only the $p$ factors $c_{ij}$ are kept ($p < 2\,m$ because one ray is composed of two sensors) which are inside the computed confidence ellipse. These $p$ factors are named $c^{\text{ellipse}}$ and satisfy $c^{\text{ellipse}} \in \mathbb{C}^p \subset \mathbb{C}^{2\,n_{\text{rays}}}$. They are represented by small green circles in Fig. 4. The $2\,n_{\text{rays}} - p$ remaining factors to be calculated are named $c^{\text{defect}}$ and are estimated as follows:

$$c^{\text{defect}} = \frac{\sum_{k=1}^{p} c_k^{\text{ellipse}}}{p}. \tag{8}$$

These three stages allow to compute all the needed calibration factors to perform baseline-free guided wave imaging with iterative HARBUT.

*Gaussian filter.* In the usual iterative HARBUT, a Gaussian blur is already applied between DT iterations. It is a kind of regularization. In this paper, a Gaussian blur is applied not only between DT iterations, but also for ray tomography. Here the importance of this filter when the number of sensors decreases is discussed.

Whether it be for ray-tomography or the DT iterations, it has been decided to adjust the Gaussian filter standard deviation to the algorithm resolution. For ray-tomography algorithms it is well known that the resolution corresponds to the first Fresnel zone $\sqrt{\lambda L}$ where $\lambda$ is the wavelength and $L$ is the propagation distance between the sensors, so for our configuration $L = 2R$ where $R$ is the radius of the sensor distribution. The effect of the defect size on the forward propagation when considering ray-theory is presented in Fig. 5 for three defects studied in Section 3. The $\sqrt{\lambda L}$ length is also plotted for scale. Regarding the HARBUT iterations (DT steps), [16] explains that the resolution of HARBUT is around 1.5-2$\lambda$ and [18] demonstrates that the spatial sampling must be carried out such that $\Delta_{\text{lim}} = \frac{\lambda}{2}$ where $\Delta_{\text{lim}}$ is the distance between two sensors. If $\Delta_{\text{lim}}$ is smaller (more sensors), the quality of the results remains the same but the computation time is increased, while if $\Delta_{\text{lim}}$ is longer (less sensors), artifacts appear caused by aliasing.

In order to eliminate non-physical oscillations (above the theoretical resolution), the Gaussian filter standard deviation is adapted as follows. A Gaussian filter is the convolution between the image data and a Gaussian of standard deviation $\sigma$. If we consider the 1-$D$ case, the Gaussian reads $f(x) \propto \exp\left(-\frac{(x-\mu)^2}{2\sigma^2}\right)$ and its Fourier transform $\hat{f}(k) \propto \sigma \exp(-ik\mu) \exp\left(-\frac{\sigma^2 k^2}{2}\right)$. The normalized Gaussian is $\hat{f}(k) = \exp\left(-\frac{k^2}{2\hat{\sigma}^2}\right) = \exp\left(-\frac{(2\pi)^2}{2\hat{\sigma}^2\lambda^2}\right)$ with $k = \frac{2\pi}{\lambda}$ and $\hat{\sigma} = \frac{1}{\sigma}$. It has been decided to fix the relative remaining spectral density to 1 % for the spatial wavelength equal to half the theoretical resolution. In practice, this means that 29.1 % of the spectral density remain for the spatial wavelength equal to the theoretical resolution. For our configuration, if $\lambda_{\text{w}}$ is the working wavelength, the theoretical ray-tomography resolution is $\sqrt{\lambda_{\text{w}} L} = \sqrt{31\,\text{mm}\,600\,\text{mm}} \approx 136\,\text{mm} \approx 4\lambda_{\text{w}}$ and the HARBUT theoretical resolution

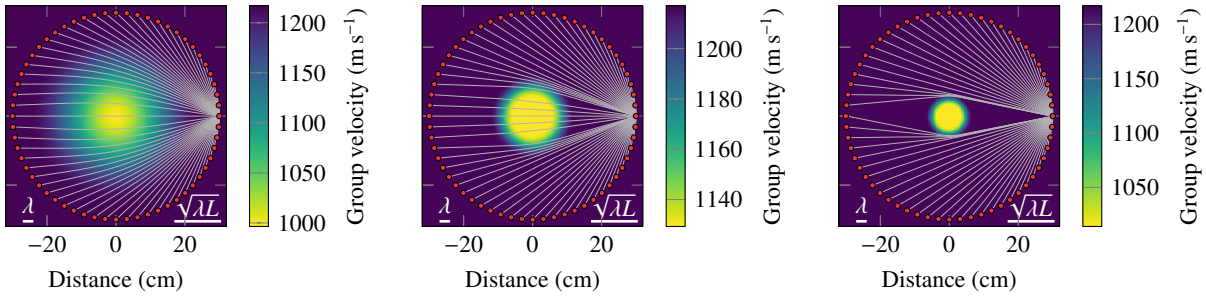


(a) Defect 1 - Only refraction phenomenon. $e_{\text{def}} = 0.7\,\text{mm}$, $r_{\text{bot}} = 0\,\text{cm}$ and $l_{\text{trans}} = 25\,\text{cm}$ (see Fig. 8 and Eq. (13) for the definitions).

(b) Defect 2 - Weak diffraction. $e_{\text{def}} = 0.3\,\text{mm}$, $r_{\text{bot}} = 5.6\,\text{cm}$ and $l_{\text{trans}} = 6.4\,\text{cm}$ (see Fig. 8 and Eq. (13) for the definitions).

(c) Defect 3 - Strong diffraction. $e_{\text{def}} = 0.65\,\text{mm}$, $r_{\text{bot}} = 3.5\,\text{cm}$ and $l_{\text{trans}} = 3\,\text{cm}$ (see Fig. 8 and Eq. (13) for the definitions).

**Fig. 5.** Forward propagation (ray-tracing) for different kinds of simulated defects.

is $2\lambda_{\text{w}}$. After some basic calculations, we find that $\sigma_{\text{ray-tomo}} = \lambda_{\text{w}}$ and $\sigma_{\text{HARBUT}} = \frac{\lambda_{\text{w}}}{2}$. When the number of sensors decreases, $\sigma_{\text{HARBUT}}$ has to be adapted according to the new value of $\Delta_{\text{lim}}$. For instance, if half the optimal theoretical number of sensors is used, the standard deviation should be $\sigma_{\text{HARBUT}} = \lambda_{\text{w}}$. It is shown in Section 3.2.2 that it is also possible to keep the standard deviation of $\frac{\lambda_{\text{w}}}{2}$ if other kinds of regularization are used.

It is worth noting that it would have also been possible to filter the disruptive spatial frequency components in the dual space ($\mathcal{K}$-space) as explained in [18], but the very smooth Gaussian filter behavior is also interesting because it acts as a relaxation in the iterative process.

We have also tried to decrease the standard deviation at every iteration. The achieved resolution is better but the image is noisier. The regularization method called "variable relaxation" presented in Section 2.2 is then needed. For the sake of simplicity, we have decided to keep a constant standard deviation for the Gaussian blur in this paper.

*Convergence criterion.* Contrary to what was used in [15], we have decided to formulate the convergence criterion using the total map (not only the damage area) to avoid problems which could occur when the noise present in the map becomes bigger than the threshold chosen to identify the defect area. The $Q$ parameter, allowing to define the convergence, then reads:

$$Q^{(n)} = \frac{\int \left| e^{(n)}(\boldsymbol{x}) - e^{(n-1)}(\boldsymbol{x}) \right| \mathrm{d}\boldsymbol{x}}{e_{\text{plt}} \int \mathrm{d}\boldsymbol{x}}, \tag{9}$$

where $e_{\text{plt}}$ is the healthy plate thickness and $e^{(n)}(\boldsymbol{x})$ is the thickness at position $\boldsymbol{x}$ for iteration $n$. Convergence is considered to be achieved when $Q \leq 2 \times 10^{-4}$, which is different from the criterion chosen in [15], and this is justified because [15] considers the defect area only. Moreover, in order to possibly work with very noisy data, another criterion is added. If $Q$ is increasing more than $M$ consecutive iterations, the algorithm stops and convergence is considered to be reached. From experience, we have observed that $M$ can be chosen to be 2 or 3.

### 2.2. Regularization

In order to perform baseline-free guided wave tomography with an undersampled sensor array, it is necessary to add prior information on the set of possible parameters $p$, otherwise the inverse problem $\Xi^{-1}$ would be ill-defined, leading to aliasing and bad convergence. This is accomplished through the use of several regularization methods [23]. Regularization is classically implemented by adding a penalty term to the Lagrangian [24]. However, this requires to explicitly formulate the tomography as a minimization problem, which adds complexity to bent ray [7] and would be impractical — if not impossible — for HARBUT. Instead, here we implement the regularization implicitly on top of the usual HARBUT algorithm, as additional steps inserted between iterations. This allows us to use the same regularization methods both for the ray and diffraction tomography steps of HARBUT.

Each regularization step operates exclusively on the partial image (weights $e_{ij}$ or map $e^{(n)}(\boldsymbol{x})$), independently of the input $\varphi_{ij}$, in an attempt to enforce some of its properties. If the prior information introduced by the implicit

regularization method accurately represents the properties of the SHM setup (such as material properties, possible defects or noise profile), it can enable us to obtain a more accurate reconstruction, or alternatively to maintain the same accuracy while using less sensors, in the spirit of sparse tomography methods [25]. On the other hand, if the prior does not faithfully represent the properties of the setup, then the regularization method can introduce a bias. It is therefore necessary to verify that the prior information is accurate for the specific SHM setup. This is done by validating the model using physical or simulated test defects, which must be representative of the expected defects when the system is later used in production. In principle, any prior can therefore be used provided that it is successfully validated. However, for the present work, we will use our knowledge of the setup to guide our choice of regularization method.

The Gaussian blur has already been presented in Section 2.1.2. Two others methods are used in this paper. The first one is based on a physical constraint: we assume that the thickness can never increase because of corrosion. This is implemented as a constant threshold equal to $e_{\text{plt}}$. The second one, which we call "variable relaxation", is inspired by Tikhonov regularization [23] (which limits the effective number of weights) and weight elimination [26] (which further reduces small weights, hence limiting noise at the cost of a lower sensitivity to small defects), and is applied to the thickness map for ray-tomography and to the object function for HARBUT after each iteration. It limits the amplification of spatial fluctuations at each iteration due to noise and the lack of sensors, while still allowing us to accurately reconstruct localized defects above the noise threshold. If we call $e_{ij}$ an element of the image, the "variable relaxation" is defined as follows:

$$e'_{ij} = \begin{cases} \tilde{e} + \dfrac{e_{ij} - \tilde{e}}{\left(1 + \frac{1}{z_{ij}^2}\right)^{\frac{\alpha}{2}}} & \text{if } 0 < \left|e_{ij} - \tilde{e}\right| < \gamma\beta\tilde{e}, \\ e_{ij} & \text{otherwise,} \end{cases} \tag{10}$$

with $e'_{ij}$ the new value of the element, $\tilde{e}$ the reference of the regularization (for example $\tilde{e} = e_{\text{plt}}$ for the ray-tomography step), $\beta \in [0, 1]$ a threshold which has to be fixed depending on the amplitude fluctuation of the noise present in the image, $\gamma \in [1, +\infty[$ a constant fixing the relaxation limit, $\alpha \in \mathbb{R}_+$ a constant defining the strength of the regularization and $z_{ij}$ reads:

$$z_{ij} = \begin{cases} \dfrac{\left|e_{ij} - \tilde{e}\right|}{\beta\tilde{e}} & \text{if } \left|e_{ij} - \tilde{e}\right| < \beta\tilde{e}, \\ \dfrac{\left|e_{ij} - \tilde{e}\right|}{\frac{1}{2}\beta\tilde{e}\left[1 - \cos\left(\pi \frac{\left|e_{ij} - \tilde{e}\right| - \gamma\beta\tilde{e}}{(1-\gamma)\beta\tilde{e}}\right)\right]} & \text{if } \beta\tilde{e} \leq \left|e_{ij} - \tilde{e}\right| < \gamma\beta\tilde{e}. \end{cases} \tag{11}$$

In order to clarify the effects of $\beta$, $\gamma$ and $\alpha$, several values are tested in Fig. 6 for a plate of thickness $e_{\text{plt}} = 2\,\text{mm}$, in the case of time-of-flight tomography.

**Domain of effect of the regularization:** The effect of the regularization is limited. Indeed, $e'_{ij} \neq e_{ij}, \forall e_{ij} \in ](1 - \gamma\beta)\tilde{e}, \tilde{e}[$ and $e'_{ij} = e_{ij}$ elsewhere. This can be verified with the red curves in Fig. 6: for the solid red line $e'_{ij} \neq e_{ij}, \forall e_{ij} \in ]0, 2[$ and $e'_{ij} = e_{ij}$ elsewhere whereas for the dashed red line $e'_{ij} \neq e_{ij}, \forall e_{ij} \in ]1, 2[$ and $e'_{ij} = e_{ij}$ elsewhere. Thereby, the domain of effect of the regularization is twice larger for the solid red line than for the dashed one.

**Effect of the threshold $\beta$:** The effect of the regularization is low for $e_{ij} \in ](1 - \gamma\beta)\tilde{e}, (1 - \beta)\tilde{e}[$ and high for $e_{ij} \in ](1 - \beta)\tilde{e}, \tilde{e}[$. To illustrate that, the solid blue line (scenario 2) and the solid red line (scenario 4) are compared. Scenarios 2 and 4 have the same regularization domain, i.e. $\gamma_2\beta_2 = \gamma_4\beta_4$, the same strength, i.e. $\alpha_2 = \alpha_4$, but two different thresholds, i.e. $\beta_2 \neq \beta_4$. We can see that the effect of the regularization is high in a larger domain for the scenario 4 than for the scenario 2. $\beta$ has to be adapted to the amplitude fluctuations of the noise present in the image. In real applications, it is possible to estimate the amplitude of the unwanted fluctuations present in the image. This noise can be due to several factors such as an error in the positioning of the sensors, a lack of sensors which causes aliasing, noise in the data or an approximation in the model. In this paper, the unwanted fluctuations have been estimated to be around 10 % of the reference thickness. So it has been decided to fix $\beta = 0.1$.

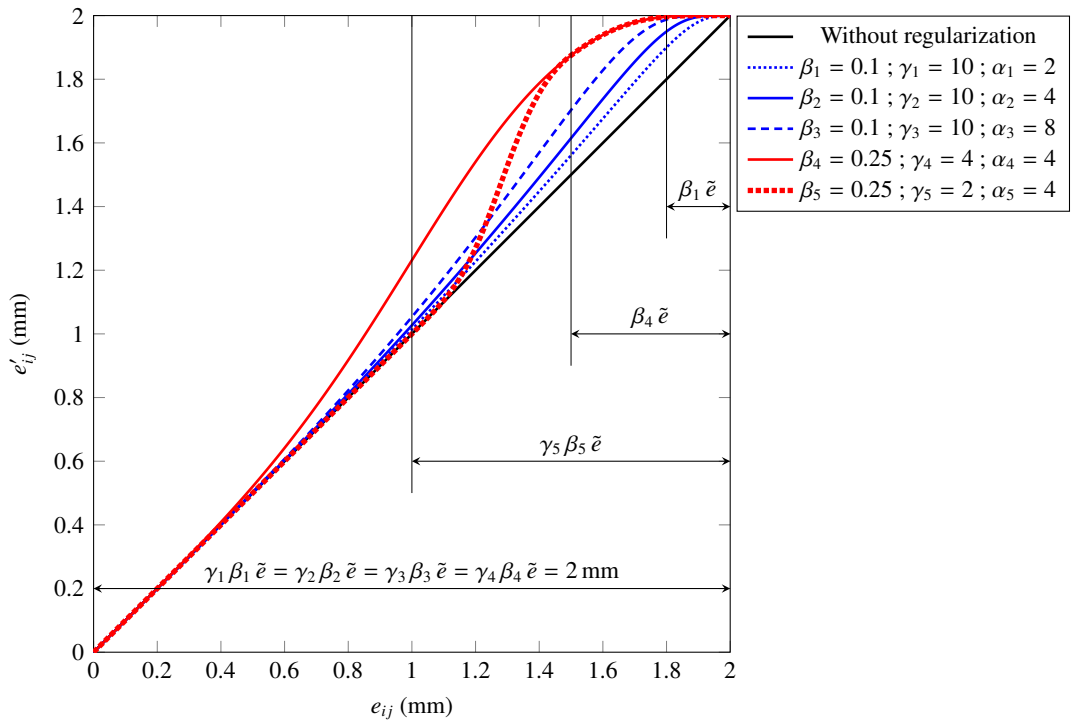


**Fig. 6.** Explanation of the regularization called "variable relaxation" for the case of time-of-flight tomography with $\tilde{e} = 2\,\text{mm}$ and different values of $\beta$, $\gamma$ and $\alpha$.

**Effect of $\alpha$:** Finally, the parameter $\alpha$ is studied thanks to the blue curves in Fig. 6. This parameter is the strength of the regularization: the higher is $\alpha$, the stronger is the effect of the regularization.

These three hyperparameters have been studied in several configurations and we have noticed that the optimal behavior is obtained when $\gamma\beta = 1$. It is interesting to note that this result allows us to fix only two parameters instead of three. We have fixed $\beta = 0.1$ as explained before. Concerning the strength, we decided to fix $\alpha = 4$ for the ray tomography because we need a very clean map for the autocalibration step, and $\alpha = 2$ for the DT step of HARBUT. We expect that hyperparameters will need to be adjusted to each specific SHM setup for optimal performance. However, as long as they only depend on the general properties of the setup, which are stable in time, our regularization method remains compatible with baseline-free tomography.

### *2.3. Global relative error*

In order to quantitatively compare tomographic images, a global relative error is used. Let $\tilde{f}_i$ be the $i^{\text{th}}$ pixel of the reference map and $f_i$ the $i^{\text{th}}$ pixel of the tomographic image. The global relative error $E_{\text{global}}$ reads:

$$E_{\text{global}} = \frac{\sqrt{\sum_{i=1}^{N_{\text{pix}}} \left(\tilde{f}_i - f_i\right)^2}}{\sqrt{\sum_{i=1}^{N_{\text{pix}}} \tilde{f}_i^2}}, \tag{12}$$

where $N_{\text{pix}}$ is the number of pixel in the image. The methods used to construct the reference maps for the numerical results and the experimental results are explained in Sections 3.1 and 4.1, respectively.

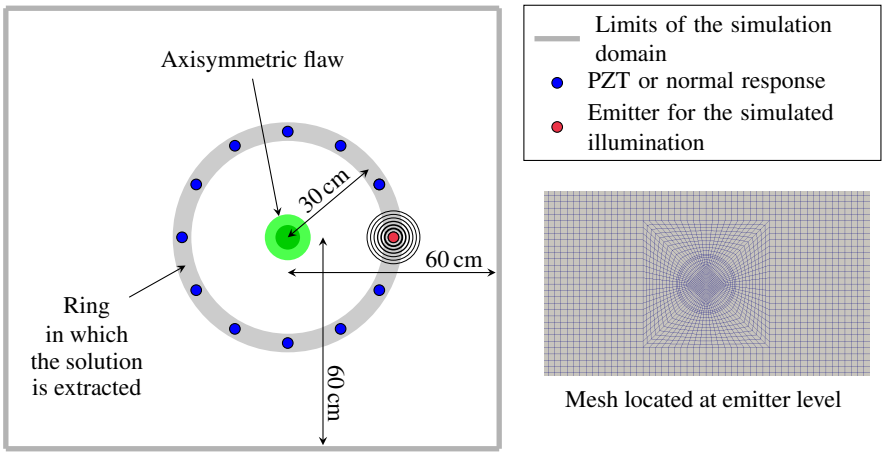


**Fig. 7.** General FEM setup.

## 3. Numerical results

### *3.1. Numerical model*

In order to test the algorithm, numerical 3D elastodynamic simulations based on the Finite Element Method (FEM) were performed. The FEM code is internally developed in the NDE department of CEA-LIST [27]. The configuration is presented in Fig. 7. An aluminum plate of density $\rho = 2.7\,\mathrm{g\,cm^{-3}}$, longitudinal velocity $V_\mathrm{L} = 6360\,\mathrm{m\,s^{-1}}$, transversal velocity $V_\mathrm{T} = 3140\,\mathrm{m\,s^{-1}}$ and dimensions $1400\,\mathrm{mm} \times 1250\,\mathrm{mm} \times 2\,\mathrm{mm}$ is considered. The sensors are positioned on a circle of radius $r_\mathrm{distrib} = 300\,\mathrm{mm}$, as shown in Fig. 7. To simulate the PZT transducer behavior, we use a second order numeric scheme both in time and in space, as well as a mesh adapted to the emitter geometry (see Fig. 7). In-plane forces normal to the circle of same diameter as the PZT disc are applied to the mesh nodes (see [28] for the modeling of PZT transducers and [29, 30] for experimental validations). The size of the elements is set to 2 mm (because the working frequency is 20.4 kHz and the associated wavelength 30.7 mm) along the two in-plane dimensions (excepted for the emitter zone). An axisymmetrical model is used in order to minimize the computation time.

The defect is parametrized using a segment $\Upsilon_\mathrm{bot}$ of length $r_\mathrm{bot}$ corresponding to the defect bottom radius, the defect depth $e_\mathrm{def}$ and a transition zone $\Upsilon_\mathrm{trans}$ of length $l_\mathrm{trans}$ defined in terms of Bernstein polynomials $b_i^{(m)}$ :

$$\begin{cases} \Upsilon_\mathrm{trans}(x_\mathrm{trans}) = e_\mathrm{plt} + e_\mathrm{def}\left(-1 + \sum_{i=0}^{3} \beta_i b_i^{(3)}\left(\frac{x_\mathrm{trans} - r_\mathrm{bot}}{l_\mathrm{trans}}\right)\right) & \forall x_\mathrm{trans} \in [r_\mathrm{bot}, r_\mathrm{bot} + l_\mathrm{trans}]\,, \\ b_i^{(m)}(x) = \frac{m!}{i!(m-i)!} x^i (1-x)^{m-i}, \end{cases} \tag{13}$$

where $\beta_0 = 0$, $\beta_1 = 0$, $\beta_2 = 1$ and $\beta_3 = 1$. With a revolution of $\Upsilon_\mathrm{bot}$ and $\Upsilon_\mathrm{trans}$ with respect to the normal axis to the plate surface and crossing the center of the sensors distribution, the defect geometry is constructed as presented in Fig. 8. The three defects studied in this paper are presented in Fig. 5.

The solution is extracted within a ring and then processed to reconstruct either the PZT response or the normal response. To obtain the normal response, we only need to interpolate the ring solution for each time-step and then extract the out-of-plane displacement for the points of interest. To compute the PZT response $f_\mathrm{PZT}^\mathrm{rec}$, it is necessary to integrate the in-plane displacements $u_1$ and $u_2$ of the active part of the PZT disc along the closed curve $\gamma_\mathrm{PZT}$:

$$f_\mathrm{PZT}^\mathrm{rec}(t) = k_\mathrm{PZT} \oint_{\gamma_\mathrm{PZT}} (\boldsymbol{u}(t) \cdot \boldsymbol{n})\, \mathrm{d}\gamma(\boldsymbol{x}), \qquad \text{where } \boldsymbol{u} \equiv (u_1, u_2) \text{ and } \boldsymbol{x} \equiv (x_1, x_2). \tag{14}$$

where $\boldsymbol{n}$ is the outer-pointing normal of $\gamma_\mathrm{PZT}$ and $k_\mathrm{PZT}$ is a constant depending on the piezoelectric material parameters (see [28] for more details). $k_\mathrm{PZT}$ is ignored here because we only need to consider relative amplitude signal variations for this work.

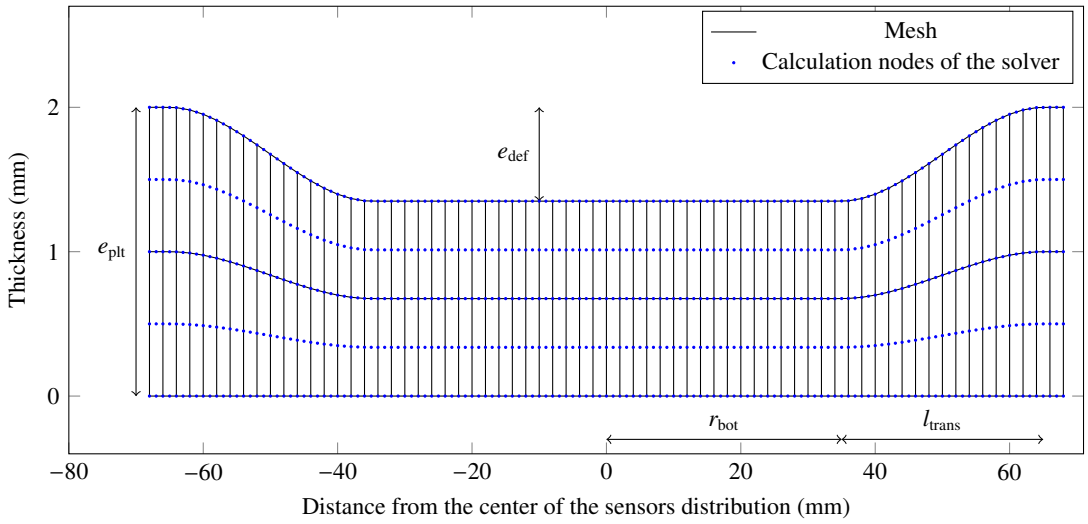


**Fig. 8.** Defect FEM setup.

The frequency behavior of a PZT transducer can be described as follows (see [29, 31] for more details):

$$\left|\hat{f}^{\text{rec}}_{\text{PZT}}(\omega)\right| \propto \left|\mathrm{J}_1\left(\pi \frac{\varnothing_{\text{PZT}}}{\lambda(\omega)}\right)\right|, \tag{15}$$

where $\varnothing_{\text{PZT}}$ is the diameter of the active part of the PZT disc and $J_1$ is the Bessel function of the first kind and of first order. Fig. 9a shows such a behavior for our setup.

Finally, before studying the algorithm behavior, experimental signals and simulated signals are compared in Fig. 9b. The excitation is a 5 cycles toneburst of central frequency 20.4 kHz. It may be noted that there is an electromagnetic coupling between the emission and the experimental measurement. The simulated normal response does not contain the $S_0$ mode. This is due to $S_0$ having practically no out-of-plane displacement in comparison with the in-plane displacement for our setup (the out-of-plane displacement is around 1 % of the in-plane displacement here). However, $S_0$ is visible in the simulated PZT response as well as in the experimental signal, both of which use the same PZT geometry. This means that, because of reflexions on the plate sides, $S_0$ will interfere with $A_0$ (the packet of interest in this paper).

### *3.2. Reconstructions*

#### *3.2.1. Ray-tomography*

In this section, we explain why straight-ray is preferred to bent-ray as a first iteration for HARBUT - which seems paradoxical given that bent-ray uses a more accurate model of wave propagation. It should be mentioned that all the ray-tomographies of Section 3 use the absolute estimator, because our final aim is to perform baseline-free guided wave tomography. Moreover, in order to avoid $S_0$ perturbations, as a first step we will only consider the normal response. Furthermore, no regularization (not even the Gaussian blur) is used in this Section.

First we consider the defect of Fig. 5a, which presents no diffraction but features strong refraction. In this particular case, Fig. 10 shows, as expected, that bent-ray gives better results than straight-ray. However, when the defect of Fig. 5c is considered, Fig. 11 shows that straight-ray has a better behavior when strong diffraction is present. This is because straight-ray is better conditioned than bent-ray. Consequently, it is sometimes better to use straight-ray instead of bent-ray, depending on the kind of defect searched for. In SHM, this problem can be overcome. Indeed, it is possible to record the reconstruction each time an inspection is performed. As the defect is growing, inspections are performed frequently enough such that the $n^{\text{th}}$ one can use the $(n-1)^{\text{th}}$ reconstructions as background, so that the Born approximation is never violated.

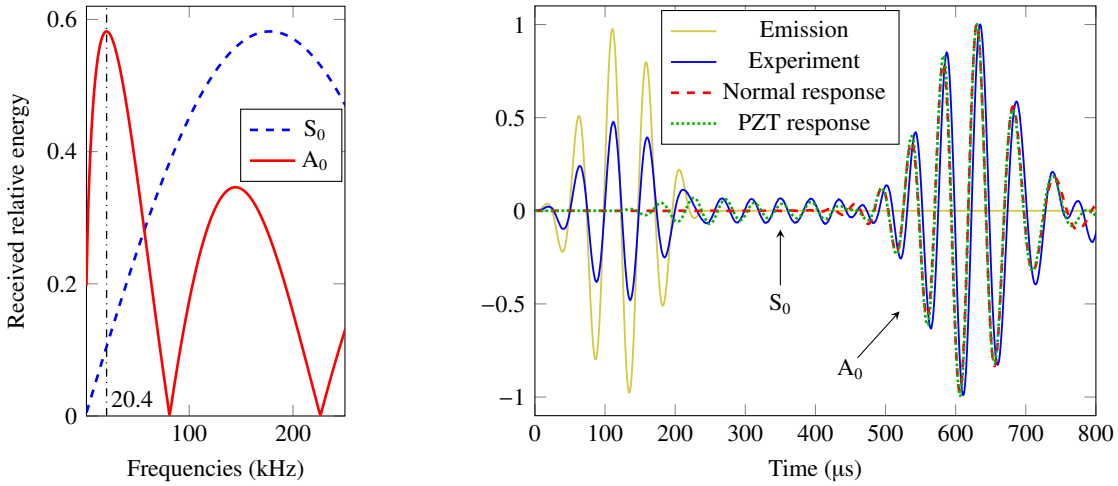


(a) Frequency filtering for a PZT transducer ($\varnothing_{PZT}$ = 18 mm) coupled to a 2 mm thickness aluminum plate.

(b) Comparison between experimental measurements and signals from the simulation.

**Fig. 9.** Validation of the simulation.

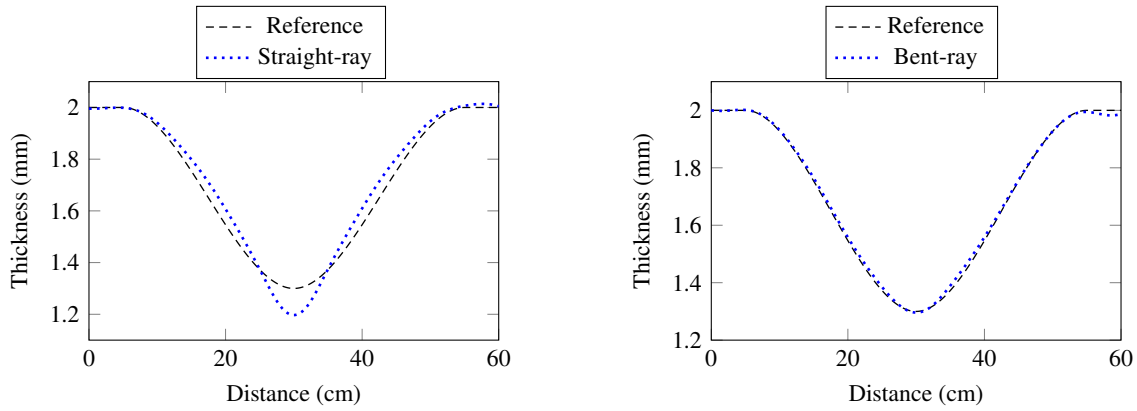


(a) Straight-ray.

(b) Bent-ray.

**Fig. 10.** Ray-tomography with refraction only (defect 1).

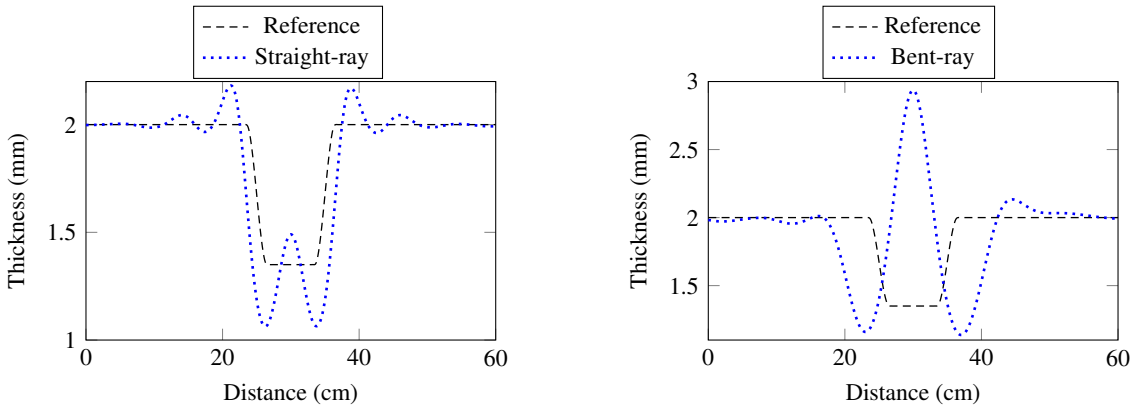


(a) Straight-ray.

(b) Bent-ray.

**Fig. 11.** Ray-tomography with strong diffraction (defect 3).

### *3.2.2. HARBUT*

*Gaussian blur effect.* The defect of Fig. 5b, presenting both refraction and diffraction, is considered. Is should be mentioned that no Gaussian blur is used for the bent-ray tomographies.

Concerning HARBUT, Fig. 12a is a reconstruction without any regularization nor Gaussian blur. We used much more sensors than the optimum number of 120 which is necessary to adequately sample the Ewald circle [18]. The algorithm has been stopped at the $7^{\text{th}}$ iteration as it would otherwise diverge. It is possible to see the $2k_0$ spatial frequency oscillations. If a Gaussian blur of standard deviation $\frac{1}{2}\lambda$ (explained in Section 2.1.2) is used, the reconstruction is practically perfect, as seen in Fig. 12b. Then, if the number of used sensors is decreased to the optimal number 120, Fig. 12c shows that the reconstruction has the same quality but the computation time is naturally lower (roughly four times faster). If half the optimal number of sensors are exploited (60) and the same Gaussian blur is applied, Fig. 12d shows again some parasitic spatial oscillations but this time of spatial wavelength longer than the ones present in Fig. 12a. If the standard deviation is increased to $1\lambda$, as explained in Section 2.1.2, these oscillations disappear but the defect reconstruction decreases in quality: see Fig. 12e. Finally, it is possible to see in Fig. 12f that by adding regularization (here, the physical threshold) and by keeping the standard deviation to $\frac{1}{2}\lambda$ for 60 sensors, we can still obtain a reconstruction of good quality.

*Baseline-free HARBUT with autocalibration method.* For the following reconstructions in this paper, only 30 sensors are used. In order to obtain the best reconstructions, we use a standard deviation of $1\lambda$ (and not $2\lambda$) with regularization, i.e. the threshold and/or the variable relaxation. Moreover, the Gaussian filter is always used for the ray-tomography reconstructions.

Baseline-free HARBUT combined with the autocalibration method and HARBUT combined with a classic calibration and with the relative estimator for the time-of-flight tomography step are compared in Fig. 13 for defect 3. Only 30 sensors are used, which corresponds to a 75 % reduction compared to optimal sampling. It should be underlined that this time the PZT response is used. Moreover, only the threshold is used (no variable relaxation). It is possible to see some small artifacts on both reconstructions due to the lack of sensors. If variable relaxation had been employed, those artifacts would have disappeared (this will be shown in the experimental Section 4.2.2). The reconstructions of Fig. 13 correspond to the calibration factors presented in Fig. 4.

Table 1 allows us to quantitatively estimate the quality of the reconstructions. The global relative error (see Eq. (12)) is very similar between the autocalibration and classic calibration methods. This study demonstrates the good performance of the autocalibration method on simulated data. The next section is dedicated to experimental studies.

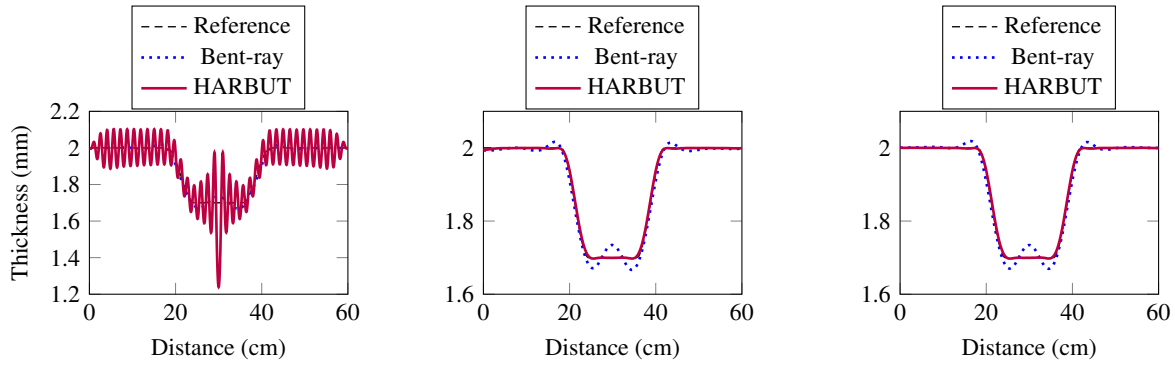


(a) HARBUT behavior for 240 sensors and without any Gaussian blur.

(b) HARBUT behavior for 240 sensors and with a Gaussian blur of standard deviation $\frac{1}{2}\lambda$.

(c) HARBUT behavior for 120 sensors and with a Gaussian blur of standard deviation $\frac{1}{2}\lambda$.

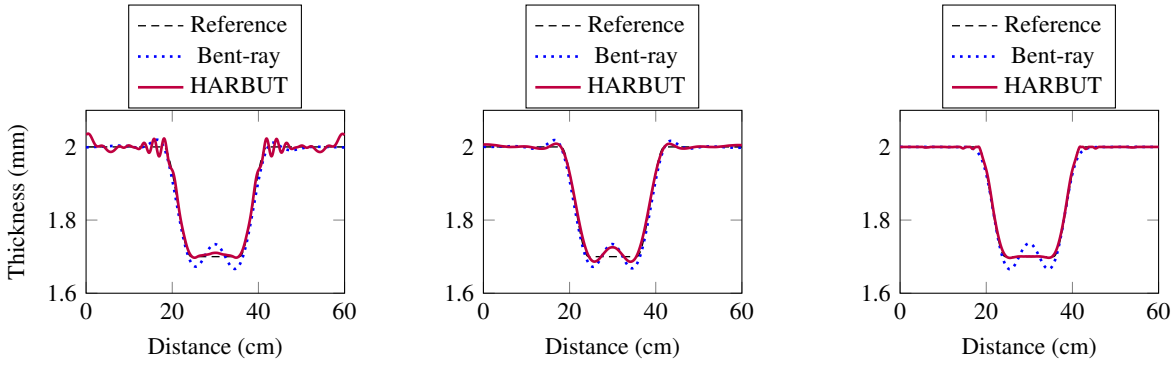


(d) HARBUT behavior for 60 sensors and with a Gaussian blur of standard deviation $\frac{1}{2}\lambda$.

(e) HARBUT behavior for 60 sensors and with a Gaussian blur of standard deviation $1\lambda$.

(f) HARBUT behavior for 60 sensors, with a Gaussian blur of standard deviation $\frac{1}{2}\lambda$ and a 2 mm threshold.

**Fig. 12.** HARBUT behavior (defect 2) as the sensor number decreases.

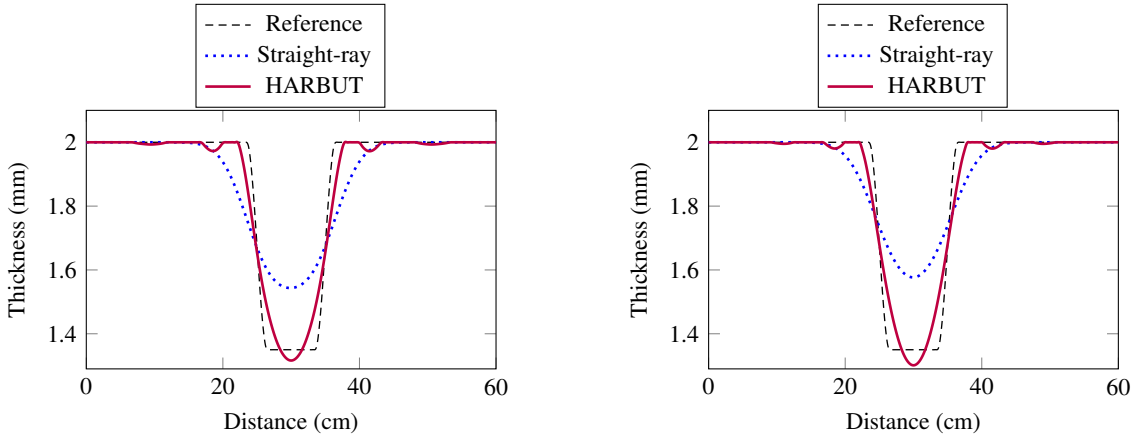


(a) Classic calibration.

(b) Autocalibration.

**Fig. 13.** Comparison between HARBUT with autocalibration and HARBUT with classic calibration (defect 3).

| | Straight-ray | HARBUT |
|---|---|---|
| Classic calibration | 1.83 % | 0.86 % |
| Autocalibration | 1.75 % | 0.83 % |

**Table 1:** Global relative error $E_{\text{global}}$ of Fig. 13 tomographies (data from simulation).

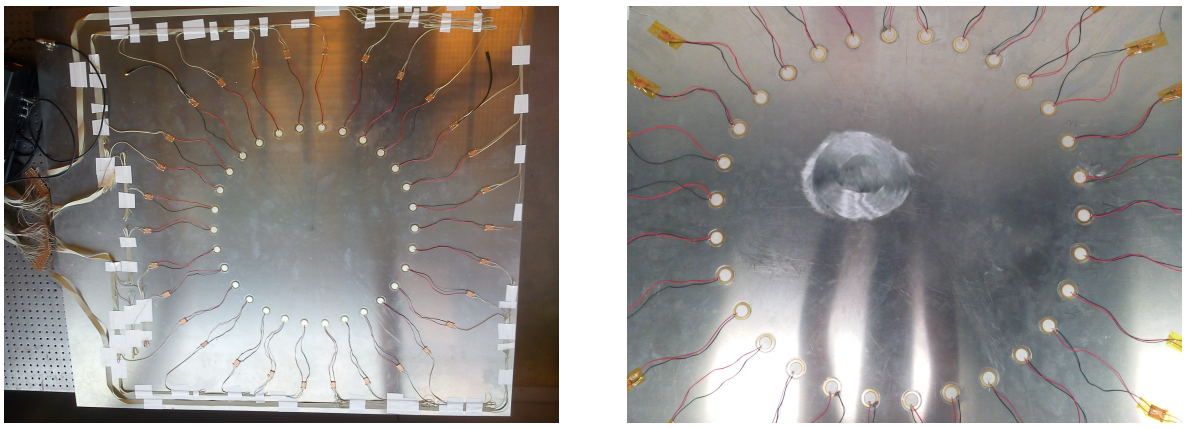

(a) Aluminum plate and PZT transducer positions.

(b) Defect position.

**Fig. 14.** Picture of the plate studied.

## 4. Experimental results

### *4.1. Experimental setup*

Two pictures of the experimental setup are showed in Fig. 14. We consider an aluminum plate of density $\rho = 2.7\,\text{g}\,\text{cm}^{-3}$, longitudinal velocity $V_\text{L} = 6360\,\text{m}\,\text{s}^{-1}$, transversal velocity $V_\text{T} = 3140\,\text{m}\,\text{s}^{-1}$ and dimensions 1400 mm × 1250 mm × 2 mm. The sensors distribution is a circle of radius $r_{\text{distrib}} = 300$ mm. The PZT transducers, of diameter $\varnothing_{\text{PZT}} = 18$ mm, are glued to the aluminum plate.

In order to have a reference to calculate the global relative error, an ultrasonic scan is performed in water immersion and the thickness map of Fig. 15 is obtained from the ToFs. The first Fresnel zone and the wavelength are superimposed on it. We can see that the defect to be imaged looks like the simulated one presented in Fig. 5c.

### *4.2. Reconstructions*

#### *4.2.1. Ray-tomography*

Here we compare the absolute estimator (Eq. (3)) to the relative estimator (Eq. (4)) in the case of experimental data.

The straight-ray reconstruction using the relative estimator is presented in Fig. 17a. The healthy part of the map is relatively "clean". When the absolute estimator is used (see Fig. 17b) the healthy part is noisier which was expected because the experimental uncertainties cannot be compensated with this estimator. However, in order to limit the noise, it is possible to apply the variable relaxation. As explained in Section 2.2, it has been decided to fix $\beta = 0.1$, the product $\gamma\beta = 1$ and $\alpha = 4$ for the ray tomography step in order to get a very clean background image for the autocalibration step. Fig. 16 shows the curve of Eq. (10) for these parameters. The resulting reconstruction is presented in Fig. 17c. This time, the healthy part contains no noise, which is essential for the following HARBUT steps.

#### *4.2.2. HARBUT*

In order to perform baseline-free HARBUT with autocalibration, the approach proposed in Section 2.1.2 to calibrate the field is applied to experimental data. First, the baseline-free straight-ray reconstruction is used to find all the healthy rays. This is presented in Fig. 18a for the full ray distribution and in Fig. 18b for the healthy rays.

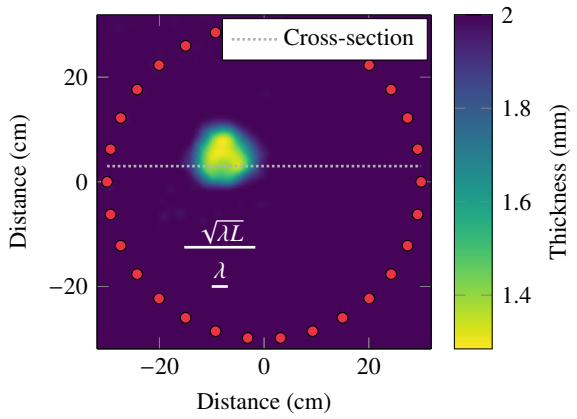


**Fig. 15.** Reference measured with an immersion ultrasonic scan.

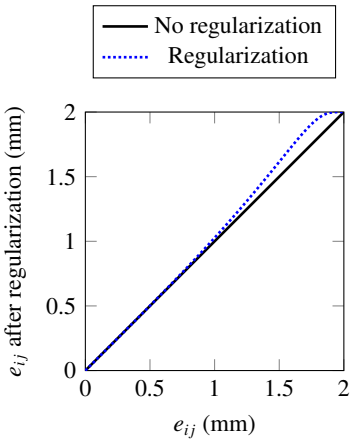


**Fig. 16.** Effect of the variable relaxation for a 2 mm thickness plate ($\beta = 0.1$, $\gamma\beta = 1$ and $\alpha = 4$). This kind of regularization is used for ray-tomography.

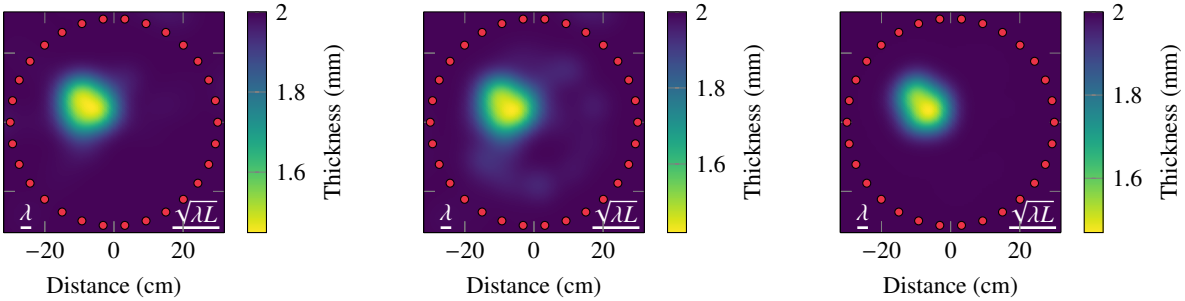


(a) Relative estimator.

(b) Absolute estimator.

(c) Absolute estimator with regularization ($\beta = 0.1$, $\gamma\beta = 1$ and $\alpha = 4$).

**Fig. 17.** Experimental straight-ray tomographies with a 2 mm threshold.

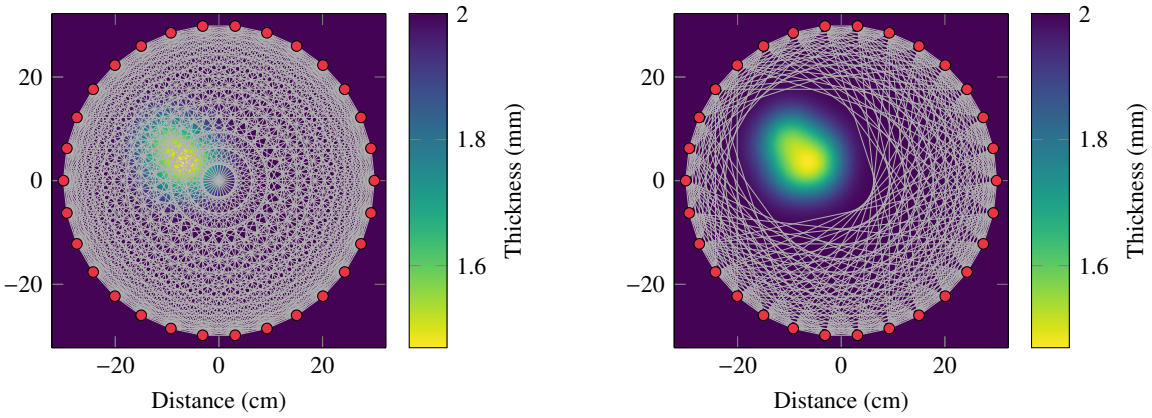


(a) Full ray distribution usually used on baseline data in order to calibrate the field for HARBUT.

(b) All the rays used in order to autocalibrate the field for baseline-free HARBUT.

**Fig. 18.** Rays crossing the defect area after straight-ray tomography reconstruction.

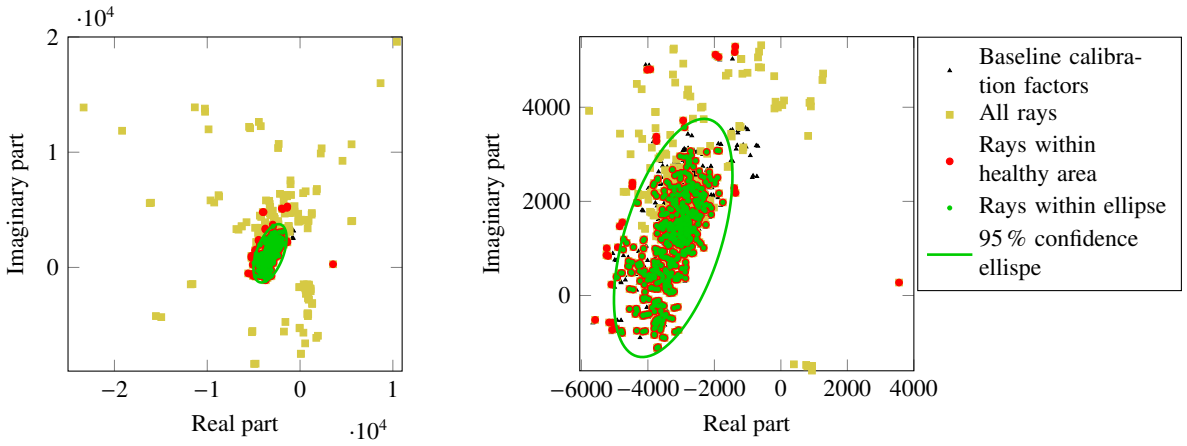


(a) All calibration factors.

(b) Zoom in on the 95 % confidence ellipse.

**Fig. 19.** Calibration factors plotted in the complex plane.

All the calibration factors are presented in Fig. 19a. This time, contrary to the axisymmetrical simulation cases, no calibration factors are superimposed on each others. Moreover, the distinction between the factors corresponding to rays crossing the defect and those travelling through the healthy part is not as clear as with simulated data. It is possible to see factors considered healthy which diverge from the proximity area. This means that the confidence ellipse visible in Fig. 19b plays a full role to remove the factors viewed as healthy but which would cause a poor calibration.

Finally, we present in Fig. 21 the results for HARBUT with the use of a baseline (all the calibration factors are calculated thanks to a baseline) and in Fig. 22 those for baseline-free HARBUT with the autocalibration method. The cross-sections plotted on the reference (see Fig. 15) are presented in Fig. 21b, 21d, 22b and 22d. Fig. 21a and 22a present the reconstructions without the variable relaxation for the DT steps. On both images, the healthy part presents artifacts because of aliasing due to the lack of sensors. By comparing cross-sections (Fig. 21b and 22b), ones can observe that the artifacts are stronger on baseline-free HARBUT with autocalibration. Fig. 21c and Fig. 22c present the reconstructions with the use of variable relaxation presented in Fig. 20a and 20b. Again, as explained in Section 2.2, it has been decided to fix $\beta = 0.1$, the product $\gamma\beta = 1$ and $\alpha = 2$ for the DT step of HARBUT. $\alpha$ does not

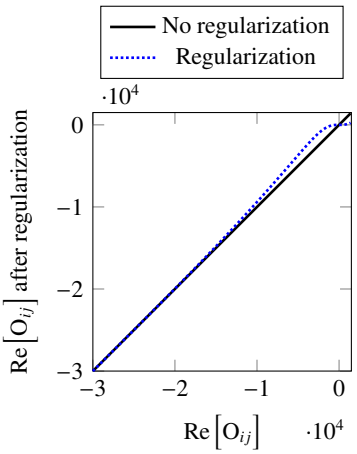


(a) Effect of the variable relaxation for the real part of O($\boldsymbol{x}$).

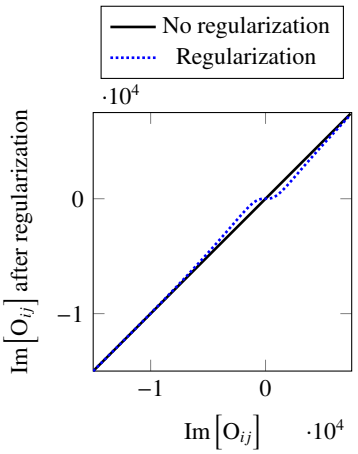


(b) Effect of the variable relaxation for the imaginary part of O($\boldsymbol{x}$).

**Fig. 20.** Effect of the variable relaxation for the DT step of HARBUT ($\beta = 0.1$, $\gamma\beta = 1$ and $\alpha = 2$).

| | Baseline | Baseline-free |
|---|---|---|
| Straight-ray | 1.56 % | 1.62 % |
| HARBUT without variable relaxation | 0.81 % | 1.20 % |
| HARBUT with variable relaxation | 0.44 % | 0.65 % |

**Table 2:** Global relative error $E_{\text{global}}$ of the tomographies of Fig. 21 and 22 (data obtained from the experience).

have to be as strong as in the case of ray tomography. The artifacts disappear almost entirely. In addition, Fig. 21d and 22d show that while small variations present in the defects (see reference) are not reconstructed because of the too large value of $\lambda$ and the lack of sensors, the global geometry is, however, well identified.

Finally, the global relative errors are presented in Table 2. This allows us to quantitatively compare the reconstructions. We can see that baseline-free HARBUT with autocalibration presents relative errors of the same order of magnitude as HARBUT with the use of a baseline for the calibration.

## 5. Discussion

The two main contributions of this paper are the autocalibration method and a way to deal with undersampled data.

Concerning the autocalibration method, one could think of a situation which could lead to poor calibration. This situation is discussed below. The autocalibration method is based on an image obtained with ray-tomography. If a transducer or a group of transducers is mispositioned, this leads to a local change in the reconstructed velocity very close to these transducers, and thus the concerned rays are not used for the autocalibration. What about the consequences of this scenario? First, in an industrial use of this method, the mispositioning is expected to be sufficiently small that it would not cause any false values within the initial image. The experimental results showed in this paper are of good quality although no particular attention has been paid to the positioning of the sensors (i.e. positioning accuracy $\approx$ 1 mm). But even if one or a group of transducers is mispositioned on purpose (or have errors), the rays concerned by the velocity change will not be used for the calibration. This is not a problem as long as there are enough rays to perform the calibration. As explained in the paragraph concerning the autocalibration, we even tried to keep only 5 % of the healthy rays (the ones which do not intersect the flaws in the ray tomography image) but the resulting image does not change significantly. Finally, the sensor positioning accuracy required to obtain a high-quality reconstruction would be enough to ensure a good autocalibration. Consequently, the autocalibration method seems to be

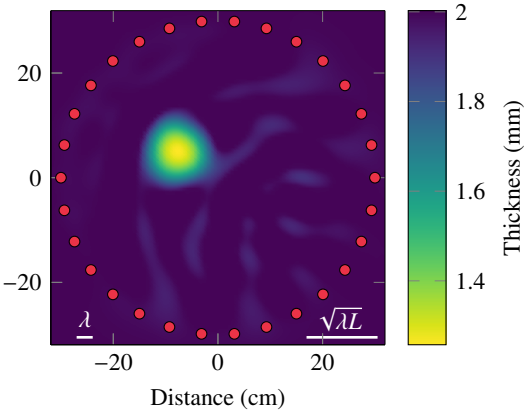


(a) No variable relaxation is used for the DT steps.

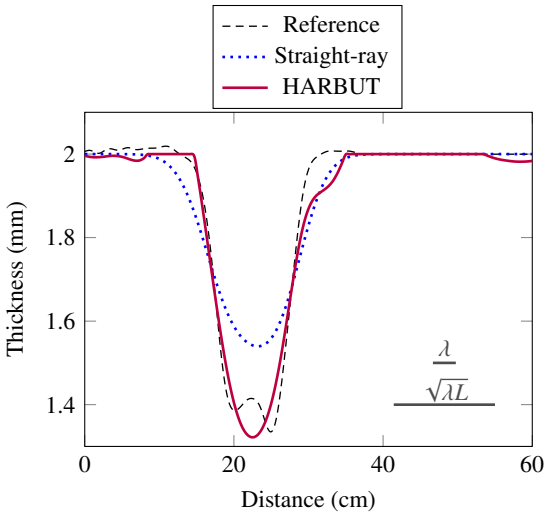


(b) Cross-section of Fig. 21a.

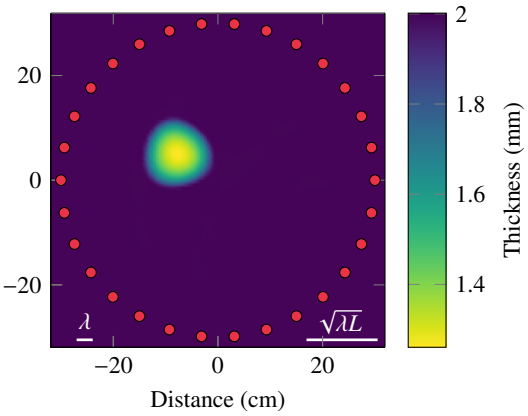


(c) Variable relaxation ($\beta = 0.1$, $\gamma\beta = 1$ and $\alpha = 2$).

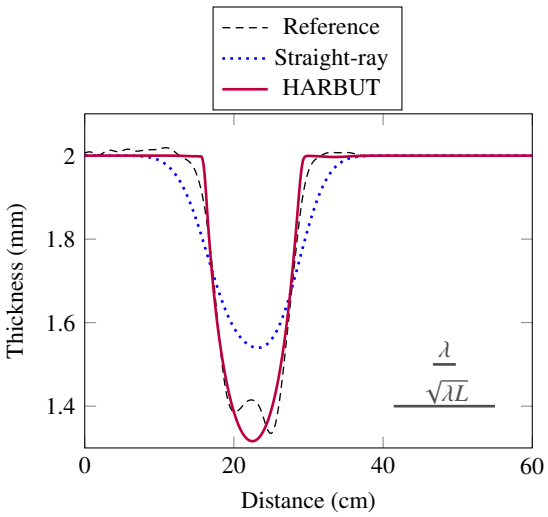


(d) Cross-section of Fig. 21c.

**Fig. 21.** Experimental HARBUT tomographies with a 2 mm threshold and using baseline data to calibrate the fields. The initial image used for iterative HARBUT is a straight-ray (relative estimator) tomography with a 2 mm threshold and with variable relaxation ($\beta = 0.1$, $\gamma\beta = 1$ and $\alpha = 4$).

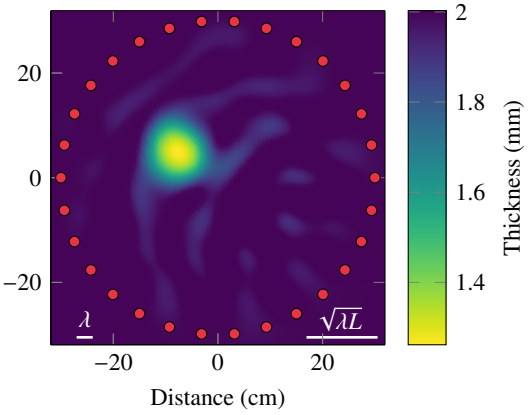


(a) No variable relaxation is used for the DT steps.

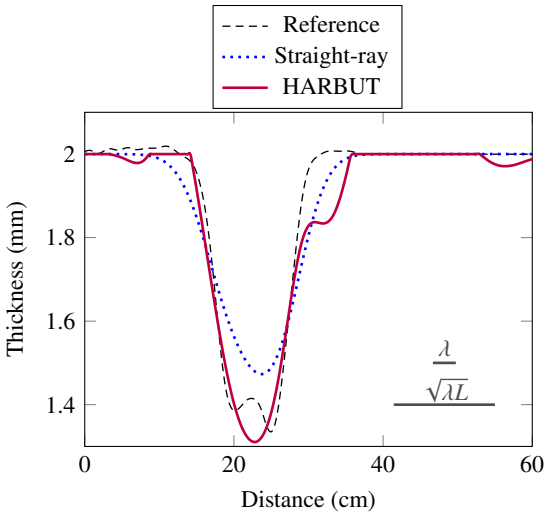


(b) Cross-section of Fig. 22a.

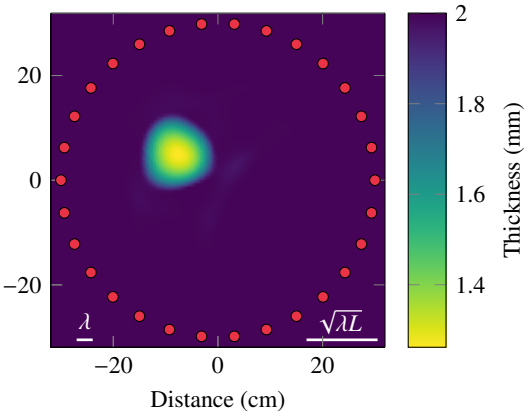


(c) Variable relaxation ($\beta = 0.1$, $\gamma\beta = 1$ and $\alpha = 2$).

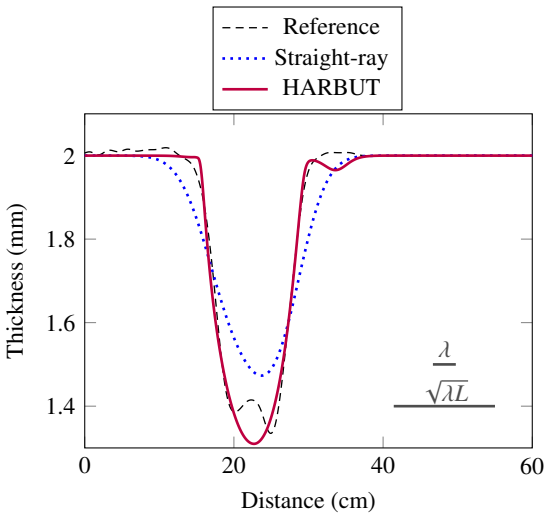


(d) Cross-section of Fig. 22c.

**Fig. 22.** Baseline-free experimental HARBUT tomographies with autocalibration and a 2 mm threshold. The initial image used for iterative HARBUT is a straight-ray (absolute estimator) tomography with a 2 mm threshold and with variable relaxation ($\beta = 0.1$, $\gamma\beta = 1$ and $\alpha = 4$).

robust enough to be used in a SHM context.

Concerning the undersampling issue, the idea was to use less sensors than the optimal number in order to be less intrusive in the structure. It has been shown in this paper that we could still obtain an image of good quality with four times less sensors than the optimal number. However, for some applications (such as aeronautics), the density of sensors required remains too high to be of practical relevance. Further studies are being conducted in parallel by the authors (and other teams) to further reduce the required number of sensors. Another promising approach is to reduce intrusiveness thanks to Fiber Bragg Gratings (FBGs). Using this technology, all the sensors can be replaced by one fiber with Bragg gratings written in the fiber. This could be a far less intrusive way to perform SHM. However, FBGs can only measure received guided waves and cannot generate them. In order to overcome this problematic the idea is to use so-called "passive methods" to retrieve the signals that are needed to perform tomography [32]. A work is conducted in parallel on passive tomography [33], and more generally on passive imaging with FBGs; it will be discussed in a future paper.

## 6. Conclusion

This paper has presented extensions to the original iterative HARBUT to deal with SHM constraints. Indeed, these extensions allow diagnostic reliability despite low sensor intrusiveness. This work focused on the use of PZT transducers which can be very intrusive when used in large numbers. It has been necessary to find a way to keep the algorithm robust when the number of sensors decreases below the optimal number which is typically required for proper sampling. In order to study a large number of configurations, a simulation campaign, which can take into account either PZT emission and reception or out-of-plane displacement, has been realized. Then, to confirm the results, experimental tomographies have been studied on real PZT data.

A method for working with a baseline-free algorithm while preserving the robustness of the calibration has been presented. This is done by using the absolute estimator for ray-tomography and an autocalibration method which is automatic, and is thus adapted to the SHM context. The absolute estimator does not compensate some systematic experimental uncertainties, which may result in a noisy map. This could make HARBUT diverge locally if this noise is too high. Moreover, it is crucial to have a clean map for the autocalibration step. In order to address this serious issue, a regularization method called variable relaxation has been developed.

Finally, because of the very low number of sensors used (four times less than the optimal number needed to reach the theoretical resolution of HARBUT) several regularizations methods have been presented. The Gaussian blur, which smoothly filters the spatial frequency components, is adjusted to the number of used sensors by tuning its standard deviation. The threshold, based on a physical constraint, allows to stabilize the reconstruction at each iteration. Lastly, the variable relaxation allows to compensate for the lack of sensors by reducing the effect of aliasing as well as the potential noise inherent to real data.

This paper has shown that it is possible to perform baseline-free HARBUT with a very low number of sensors compared to the optimal number, but this is at the expense of resolution. Future work could be performed to maintain a relatively good resolution even with a low number of sensors. Compressed sensing seems to be a promising tool for that purpose [25]. Moreover, recently Shi and Huthwaite worked on the undersampled diffraction tomography problematic in the case of a 50 % reduction of the number of sensors. The idea is to use a forward model to get virtual transducers measurements in an iterative approach and so improve the imaging resolution [34].

Another approach would be to use less intrusive sensors. For instance, Fiber Bragg Gratings (FBGs) is a promising solution to increase the number of measurement points without increasing the intrusiveness of the system. However, unlike PZT transducers generally used in SHM, FBGs cannot emit elastic waves. This shortcoming can be circumvented by employing passive methods in order to retrieve the Green's function from elastic diffuse fields — naturally present in structures — measured simultaneously between two sensors [32, 33, 35].

Work is being conducted by the authors in parallel on passive tomography and will be discussed in a future paper. A longer-term program consists in performing passive tomography with FBGs only, in order to use a sufficient number of sensors to reach the maximum achievable resolution by the HARBUT algorithm.

## References

[1] Guidelines for implementation of structural health monitoring on fixed wing aircraft, Tech. rep., SAE International (2013).

[2] D. Jansen, D. Hutchins, Lamb wave tomography, Ultrasonics symposium (1990) 1017–1020.
[3] J. McKeon, M. Hinders, Parallel projection and crosshole Lamb wave contact scanning tomography, Acoustical Society of America 106 (5) (1999) 2568–2577.
[4] E. Malyarenko, M. Hinders, Fan beam and double crosshole Lamb wave tomography for mapping flaws in aging aircraft structures, Journal of the Acoustical Society of America 108 (2000) 1631–1639.
[5] P. Belanger, P. Cawley, Feasibility of low frequency straight-ray guided wave tomography, NDT&E International 42 (2009) 113–119.
[6] S. Li, K. Mueller, M. Jackowski, D. Dione, L. Staib, Fast marching method to correct for refraction in ultrasound computed tomography, 3rd IEEE International Symposium on Biomedical Imaging: Nano to Macro (2006) 896–899.
[7] A. Hormati, I. Jovanović, O. Roy, M. Vetterli, Robust ultrasound travel-time tomography using the bent ray model, in: Medical Imaging 2010: Ultrasonic Imaging, Tomography, and Therapy, Vol. 7629, International Society for Optics and Photonics, 2010, p. 76290I.
[8] S. Li, M. Jackowski, D. Dione, T. Varslot, L. Staib, K. Mueller, Refraction corrected transmission ultrasound computed tomography for application in breast imaging, Medical Physics 37 (2010) 2233–2246.
[9] C. Willey, F. Simonetti, P. Nagy, G. Instanes, Guided wave tomography of pipes with high-order helical modes, NDT & E International 65 (2014) 8–21.
[10] C. Wang, L. Rose, Plate-wave diffraction tomography for structural health monitoring, Review of Quantitative Nondestructive Evaluation 22 (2003) 1615–1622.
[11] F. Simonetti, N. Huang, From beamforming to diffraction tomography, Applied Physics 103 (2008) 103–110.
[12] A. Rohde, M. Veidt, L. Rose, J. Homer, A computer simulation study of imaging flexural inhomogeneities using plate-wave diffraction tomography, Ultrasonics 48 (2007) 6–15.
[13] P. Belanger, P. Cawley, F. Simonetti, Guided wave diffraction tomography within the Born approximation, IEEE Transactions on Ultrasonics, Ferroelectrics, and Frequency Control 57 (6) (2010) 1405–1418.
[14] P. Müller, M. Schürmann, J. Guck, The theory of diffraction tomography, arXiv preprint arXiv:1507.00466.
[15] P. Huthwaite, F. Simonetti, High-resolution guided wave tomography, Wave Motion 50 (2013) 979–993.
[16] P. Huthwaite, Evaluation of inversion approaches for guided wave thickness mapping, Proceedings of the Royal Society A 470 (2014) 20140063.
[17] P. Huthwaite, Improving accuracy through density correction in guided wave tomography, Proceedings of the Royal Society of London A: Mathematical, Physical and Engineering Sciences 472 (2016) 20150832. doi:10.1098/rspa.2015.0832.
[18] P. Huthwaite, Eliminating incident subtraction in diffraction tomography, Proceedings of the Royal Society of London A: Mathematical, Physical and Engineering Sciences 472 (2016) 20160707. doi:10.1098/rspa.2016.0707.
[19] P. Huthwaite, A. Zwiebel, F. Simonetti, A new regularization technique for limited-view sound-speed imaging, IEEE Transactions on Ultrasonics Ferroelectrics and Frequency Control 60 (3) (2013) 603–613.
[20] P. Huthwaite, Guided wave tomography with an improved scattering model, Proceedings of the Royal Society of London A: Mathematical, Physical and Engineering Sciences 472 (2016) 20160643. doi:10.1098/rspa.2016.0643.
[21] A. Kak, M. Slaney, Principles of Computerized Tomographic Imaging, IEEE Press, New York, 1988.
[22] M. Unser, Splines: A perfect fit for signal and image processing, IEEE Signal processing magazine 16 (6) (1999) 22–38.
[23] A. N. Tikhonov, Solution of incorrectly formulated problems and the regularization method, Soviet Math. Dokl. 4 (1963) 1035–1038.
[24] D. Wysoczański, J. Mroczka, A. Polak, Performance analysis of regularization algorithms used for image reconstruction in computed tomography, Bulletin of the Polish Academy of Sciences Technical Sciences 61 (2) (2013) 467–474.
URL https://content.sciendo.com/view/journals/bpasts/61/2/article-p467.xml
[25] H. Wang, Méthodes de reconstruction d'images à partir d'un faible nombre de projections en tomographie par rayons x [in french], Ph.D. thesis, Université de Grenoble (2011).
[26] A. S. Weigend, D. E. Rumelhart, B. A. Huberman, Generalization by weight-elimination with application to forecasting, in: R. P. Lippmann, J. E. Moody, D. S. Touretzky (Eds.), Advances in Neural Information Processing Systems 3, Morgan-Kaufmann, 1991, pp. 875–882.
[27] A. Imperiale, S. Chatillon, P. Calmon, N. Leymarie, S. Imperiale, E. Demaldent, UT Simulation of Embedded Parametric Defects Using a Hybrid Model Based Upon Spectral Finite Element and Domain Decomposition Methods, in: 19th World Conference on Non-Destructive Testing, 2016.
[28] E. Fribourg-Blanc, Actionneurs en couches minces pour le contrôle santé de structures aéronautiques - étude de films de PZT et de PMNT [in french], Ph.D. thesis, Université de Valenciennes et du Hainaut-Cambrésis (2003).
[29] B. Chapuis, Contrôle santé intégré par méthode ultrasonore des réparations composites collées sur des structures métalliques [in french], Ph.D. thesis, Université Paris 7 - Denis Diderot (2010).
[30] N. Etaix, A. Leblanc, M. Fink, R.-K. Ing, Thickness or phase velocity measurements using the Green's function comparison method, IEEE transactions on ultrasonics, ferroelectrics, and frequency control 57 (8).
[31] V. Giurgiutiu, Tuned Lamb wave excitation and detection with piezoelectric wafer active sensors for structural health monitoring, Journal of Intelligent Material Systems and Structures 16 (2005) 291–305.
[32] T. Druet, B. Chapuis, M. Jules, G. Laffont, E. Moulin, Passive guided waves measurements using fiber Bragg gratings sensors, The Journal of the Acoustical Society of America 144 (3) (2018) 1198–1202. doi:10.1121/1.5054015.
[33] T. Druet, Passive guided wave tomography for structural health monitoring applications [in french], Ph.D. thesis, Université de Valenciennes et du Hainaut-Cambresis (2017).
[34] F. Shi, P. Huthwaite, Ultrasonic wave-speed diffraction tomography with undersampled data using virtual transducers, IEEE Transactions on Ultrasonics, Ferroelectrics, and Frequency Control.
[35] T. Druet, B. Chapuis, P. Calmon, E. Moulin, Feasibility of passive SHM for corrosion detection by guided wave tomography, in: 19th World Conference on Non-Destructive Testing, 2016.